

# Assembly bias evidence in close galaxy pairs

I. Ferreras<sup>1,2,3,4\*</sup>, A. M. Hopkins<sup>5</sup>, C. Lagos<sup>6</sup>, A. E. Sansom<sup>7</sup>, N. Scott<sup>8,9</sup>,  
S. M. Croom<sup>8,9</sup>, S. Brough<sup>10</sup>

<sup>1</sup> Mullard Space Science Laboratory, University College London, Holmbury St Mary, Dorking, Surrey RH5 6NT, UK

<sup>2</sup> Department of Physics and Astronomy, University College London, Gower Street, London WC1E 6BT, UK

<sup>3</sup> Instituto de Astrofísica de Canarias, Calle Vía Láctea s/n, E38205, La Laguna, Tenerife, Spain

<sup>4</sup> Departamento de Astrofísica, Universidad de La Laguna (ULL), E-38206 La Laguna, Tenerife, Spain

<sup>5</sup> Australian Astronomical Optics, Macquarie University, 105 Delhi Rd, North Ryde, NSW 2113, Australia

<sup>6</sup> ICRAR, M468, University of Western Australia, 35 Stirling Hwy, Crawley, WA 6009, Australia

<sup>7</sup> Jeremiah Horrocks Institute, University of Central Lancashire, Preston PR1 2HE, UK

<sup>8</sup> Sydney Institute for Astronomy, School of Physics, A28, The University of Sydney, Sydney, NSW 2006, Australia

<sup>9</sup> ARC Centre of Excellence for All Sky Astrophysics in 3 Dimensions (ASTRO 3D)

<sup>10</sup> School of Physics, University of New South Wales, NSW 2052, Australia

MNRAS, in press. Accepted 2019 May 6. Received 2019 March 20; in original form 2018 December 17

## ABSTRACT

The growth channel of massive galaxies involving mergers can be studied via close pairs as putative merger progenitors, where the stellar populations of the satellite galaxies will be eventually incorporated into the massive primaries. We extend our recent analysis of the GAMA-based sample of close pairs presented in Ferreras et al. to the general spectroscopic dataset of SDSS galaxies (DR14), for which the high S/N of the data enables a detailed analysis of the differences between satellite galaxies with respect to the mass of the primary galaxy. A sample of approximately two thousand satellites of massive galaxies is carefully selected within a relatively narrow redshift range ( $0.07 < z < 0.14$ ). Two main parameters are considered as major drivers of the star formation history of these galaxies, namely: the stellar velocity dispersion of the satellite ( $\sigma$ ), as a proxy of “local” drivers, and the ratio between the stellar mass of the satellite and the primary,  $\mu = M_{\text{SAT}}/M_{\text{PRI}}$ , meant to serve as an indicator of environment. Consistently with the independent, GAMA-based work, we find that satellites around the most massive primaries appear older, at fixed velocity dispersion, than satellites of lower mass primaries. This trend is more marked in lower mass satellites ( $\sigma \sim 100 \text{ km s}^{-1}$ ), with SSP-equivalent age differences up to  $\sim 0.5 \text{ Gyr}$ , and can be interpreted as a one-halo assembly bias, so that satellites corresponding to smaller values of  $\mu$  represent older structures, akin to fossil groups.

**Key words:** galaxies: evolution – galaxies: formation – galaxies: interactions – galaxies: stellar content.

## 1 INTRODUCTION

A wide range of factors determine the formation of galaxies, as they evolve from clumps of gas that follow the original density fluctuations at early times to the complex web of galaxies that we see today. One can separate potential mechanisms that influence galaxy formation and evolution between local (short-range” mechanisms that extend over  $\sim 1\text{--}10 \text{ kpc}$  scales) and global ones (environment-related processes that can affect galaxy formation over much larger scales). Alternatively, one can look into the formation of

galaxies as a “two stage” process (Oser et al. 2012), distinguishing between an in-situ formation phase – from the collapse of gas and subsequent cooling into the newly forming galaxy – and an ex-situ component made up of stars formed in other galaxies, accreted through merging. This split is especially informative in massive galaxies (defined as those having a stellar mass higher than  $\sim 10^{11} M_{\odot}$ ), as the massive cores of these galaxies feature old, metal-rich and  $[\alpha/\text{Fe}]$  overabundant populations (e.g. Thomas et al. 2005; de La Rosa et al. 2011), as expected from an early, strong, and short-lived episode of formation. This pattern of ages and abundances in massive galaxies is suggestive of a substantial contribution from the in-situ phase. In con-

\* E-mail: iferreras@iac.es

trast, numerical simulations indicate that the outer envelope may be built up through the ex-situ growth channel (e.g. Naab et al. 2009). Radial gradients of stellar populations in massive galaxies, therefore, allow us to understand the role of these two phases in the formation of massive galaxies at present time. For instance, early-type galaxies show a strong negative metallicity gradient but a relatively shallow age profile (e.g. La Barbera et al. 2012; Greene et al. 2015; Goddard et al. 2016). The outer regions of massive galaxies also have enhanced  $[\alpha/\text{Fe}]$  ratios, indicative of short star-formation timescales, ceasing at early times (Greene et al. 2013, 2015). Therefore, taking the outer regions of massive galaxies as constituted by the ex-situ phase, we would infer that the progenitors that feed this phase are low-metallicity (i.e. potentially low mass) galaxies formed at early times. Is it possible to view this external envelope dein the making?

Observations of close pairs allow us to probe the progenitors of eventual galaxy mergers (e.g. Patton et al. 2000; Lin et al. 2004; Sol Alonso et al. 2004; Ellison et al. 2008; Rogers et al. 2009; López-Sanjuan et al. 2012; Mármol-Queralto et al. 2012). By choosing a relatively small separation, both spatially (in projection) and in velocity (along the line of sight), it is possible to identify systems dynamically bound and potentially merging. This technique can be exploited to determine merger rates, assess feedback effects and study the properties of the progenitors that will form the future, merged, system (see the above references for a non-extensive selection of results). In Ferreras et al. (2014) a sample of  $z \lesssim 1.5$  massive galaxies was selected from the SHARDS deep, medium-band survey (Pérez-González et al. 2013) to assess the growth of the ex-situ phase as a function of the merger ratio. A dominant contribution was found from mergers with satellite-to-primary mass ratio in the range  $\mu \equiv M_{\text{SAT}}/M_{\text{PRI}} = [0.5, 1]$ , i.e. putting the contribution of minor mergers in a subdominant category. This result was found to hold at lower redshift, as presented in the SDSS-based study of Ruiz et al. (2014). Note that we should not extrapolate this trend to the general population of (lower mass) galaxies, where minor merging can dominate the ex-situ phase (e.g. Kaviraj 2014). A follow-up study selecting close pairs involving, at least, a massive galaxy was undertaken in the Galaxy And Mass Assembly (GAMA) survey (Driver et al. 2011), where the high completeness of the survey and the availability of optical spectroscopy – mostly from the Anglo-Australian Telescope (AAT) – allowed us to perform an unbiased search of variations in the stellar populations of the merger progenitors (Ferreras et al. 2017). An intriguing segregation was found so that, at fixed stellar mass, satellites orbiting the most massive galaxies were, on average, 1 Gyr older than those around the lower mass primaries. This effect was found not to depend on whether the stellar mass of the primary or the hosting halo mass is used to split the sample. This result is reminiscent of galactic conformity, i.e. the tendency for the age of a galaxy to align with the age of the corresponding central galaxy (Weinmann et al. 2006; Hartley et al. 2015; Kawinwanichakij et al. 2016), and leads to the concept of galaxy conformity (see Wechsler & Tinker 2018, for a recent review). A common interpretation of galaxy conformity is that it could be driven by assembly bias (Gao, Springel, & White 2005), that refers to the effect of halos in higher density environment being older and more concentrated at fixed stellar mass (Hearin et al. 2015). In

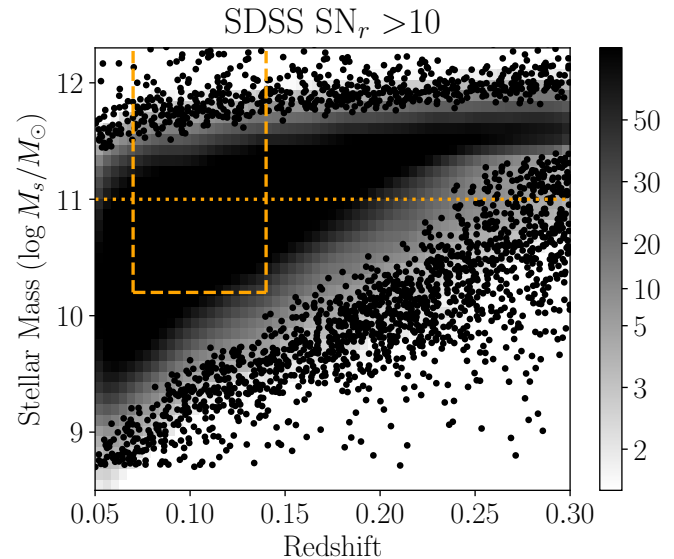


**Figure 1.** Density plot showing the number of available SDSS spectra on a stellar mass vs redshift diagram. The greyscale is applied to the region of high density of spectra, whereas in the lower density regions the individual data points are shown as dots. The dashed lines mark the region from which the final sample of close pairs is extracted (see Fig. 2 and text for details). For reference, all primary galaxies are located above the horizontal dotted line.

the latter scenario, galaxy properties would depend on halo properties beyond its virial mass. There are contradictory results in the literature as to whether assembly bias is at the heart of galaxy conformity (e.g., Treyer et al. 2018) or is due to internal physical processes in halos that are unrelated to halo age (e.g., Zu & Mandelbaum 2018). In simulations, however, the connection between conformity and assembly bias is more clearly established (e.g., Bray et al. 2016; Paranjape et al. 2015; Pahwa & Paranjape 2017). Observational studies of this bias provide valuable clues about the interplay between structure formation, driven by dark matter, and galaxy formation, which strongly depends on a plethora of physical processes termed ‘baryon physics’.

In this paper we extend the analysis presented in Ferreras et al. (2017) by exploring an independent sample from the Sloan Digital Sky Survey (SDSS, York et al. 2000). This work, therefore, focuses on close pairs involving at least a massive galaxy, and the potential effect that a massive primary, or its environment, could exert on the associated satellite. The larger data volume probed by the SDSS and the exquisite flux calibration allow us to revisit the question of whether there are substantial differences in the stellar populations of satellites orbiting massive galaxies and to produce a more accurate estimate of the stellar age differences, and a more comprehensive analysis of possible biases due to the sample selection. A standard  $\Lambda$ CDM cosmology is adopted, with  $\Omega_m = 0.27$  and  $H_0 = 70 \text{ km s}^{-1} \text{ Mpc}^{-1}$ . For reference, the look-back time to  $z=0.1$  (roughly the median of our working sample) is 1.30 Gyr and the 3 arcsec diameter fibre of the SDSS spectrograph maps into a projected distance of 5.5 kpc at that redshift.

## 2 SDSS SAMPLE SELECTION

We retrieve from the Sloan Digital Sky Survey (SDSS) DR14 archive (Abolfathi et al. 2018) all spectra from the classic SDSS database, classified as a galaxy, in the redshift range  $0.05 < z < 0.3$ , and with a SNR in the  $r$  band above 10.0. Moreover, we reject data with a raised zWARNING flag. The spectra was cross-matched with the Johns Hopkins/MPA catalogue to retrieve the stellar masses, based on methods set out in Kauffmann et al. (2003). The resulting sample comprises 531,280 spectra. Fig. 1 illustrates the stellar mass completeness of the full set, by showing the number of available SDSS galaxy spectra on a diagram of stellar mass versus redshift (in regions with lower numbers of available spectra the shaded representation is substituted by individual data points). The dashed lines delimit the range in redshift and stellar mass probed in this sample (see below). From this sample, we select all massive galaxies, defined as having a stellar mass above  $10^{11} M_{\odot}$  (i.e. above the horizontal dotted line in Fig. 1). The resulting sample of 186,824 massive galaxies is then searched for the availability of SDSS spectra of nearby galaxies – selected from the parent sample of high SNR data – located within a projected radius of 100 kpc and with a peculiar velocity, derived from the redshift difference, within  $\pm 700$  km/s. We note this is the same criterion applied to our GAMA-based sample of close pairs, as presented in Ferreras et al. (2017).

Fig. 2 shows the general sample on a diagram plotting the stellar mass ratio ( $\mu \equiv M_{\text{SAT}}/M_{\text{PRI}}$ ) vs redshift. The selection effect is apparent, with a strong Malmquist bias towards higher masses at higher redshift, as expected since the SDSS spectroscopic survey is limited to  $r < 17.7$  AB mag. Moreover, our high S/N constraint accentuates the effect of the bias. Therefore, a naive adoption of all spectra as shown by the grey dots will introduce a systematic, such that at high  $\mu$ , we would be selecting a wide range of redshifts, whereas satellite spectra corresponding to low  $\mu$  only probe the lower redshift subset. Furthermore, the wide redshift covered introduces an additional bias due to the fixed aperture imposed by the 3 arcsec fibres of the SDSS spectrograph. Over the full  $z=0.05$ – $0.3$  redshift interval shown in the figure, the fibre maps a physical size between 2.9 and 13.3 kpc. The presence of population gradients will therefore produce an additional systematic trend.

In order to mitigate these possible biases, we restrict the redshift range to  $z=0.07$ – $0.14$  (cyan dashed lines in Fig. 1, and orange box in Fig. 2). Note that within the range of redshift and stellar mass probed here, we do not expect an incompleteness from the flux limit of the parent sample. The inset in Fig. 2 shows our working sample on a diagram with stellar mass ratio vs velocity dispersion. We impose a further constraint by restricting the sample in velocity dispersion between 100 and 250  $\text{km s}^{-1}$ , splitting the interval into five equal steps of width  $\Delta\sigma=30 \text{ km s}^{-1}$ . We choose galaxies with mass ratios  $\log \mu > -0.8$ , and split the sample into three terciles, where the highest and lowest bins are colour coded in blue ( $\mu_1$ ) and red ( $\mu_3$ ), respectively. Table 1 shows the details of the stacks. Taking all galaxies within our working sample regardless of the stellar mass ratio, i.e. the  $\mu_0$  subset in Table 1, we obtain a median redshift  $z_M = 0.11 \pm 0.02$ , which implies a variation in the physical extent of the SDSS spectroscopic fibre of  $\sim \pm 1$  kpc.

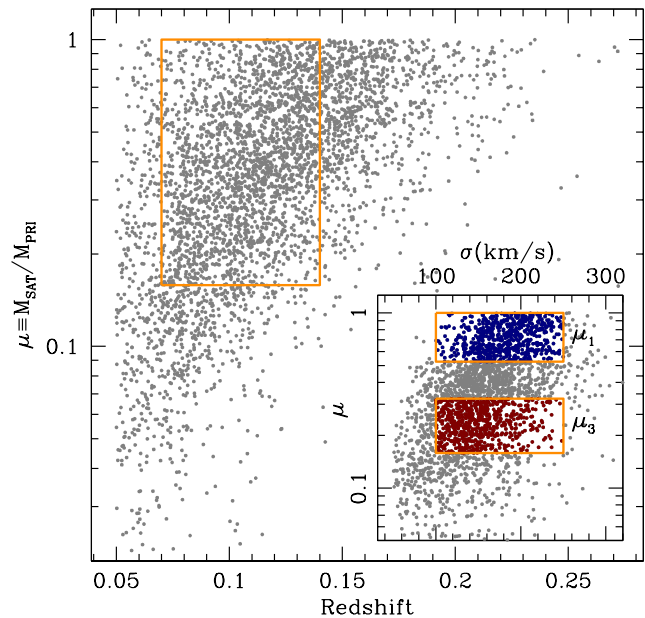


**Figure 2.** This figure illustrates the stacking strategy. The grey dots show the distribution of redshift vs stellar mass ratio for the starting sample of close pair systems. The orange box encloses the narrower redshift interval ( $0.07 < z < 0.14$ ) over which we can probe a wide range of mass ratios ( $\log \mu \geq -0.8$ ). The inset shows the sample within this redshift and mass ratio window, with respect to velocity dispersion, our “local proxy”. The interval  $100 < \sigma < 250 \text{ km s}^{-1}$  is further divided into three terciles with respect to the mass ratio, from which we extract the highest (i.e. major merger progenitor) and the lowest (i.e. minor merger progenitor) terciles, as shown in blue (top box,  $\mu_1$ ) and red (bottom box,  $\mu_3$ ), respectively.

## 3 STACKING PROCEDURE

Following Ferreras et al. (2017), the SDSS spectra are stacked following two main parameters, one describing the “local” driver of formation, and a second one related to the presence of the pair. For the former, we choose the velocity dispersion, and for the latter, we choose the stellar mass ratio,  $\mu$ , as defined above. We use the SDSS official estimates of velocity dispersion, as provided by the DR14 (Abolfathi et al. 2018) SPECOBJ catalogue (parameter velDisp). Note that, in contrast to this work, Ferreras et al. (2017) used the stellar mass of the satellite galaxy instead of velocity dispersion. The main reason to choose stellar mass was the inherently larger uncertainty in the estimate of velocity dispersion because of the lower S/N of the spectra. However, the velocity dispersion correlates strongly with the population properties such as observed colour, age, metallicity or  $[\alpha/\text{Fe}]$  (see, e.g., Bernardi et al. 2003; Thomas et al. 2005; Graves, Faber, & Schiavon 2009; Scott et al. 2017; Barone et al. 2018), and provides a better tracer of the underlying stellar populations, whereas the stellar mass is not so strongly correlated with population properties. In the discussion section, we will elaborate on the differences between these two choices of a local driver.

All spectra are corrected for foreground (Milky Way) dust extinction – following the standard extinction law of Cardelli, Clayton, & Mathis (1989), with the colour excess

**Table 1.** Number and S/N (in brackets) of spectra used in the stacks (see Fig. 2). The S/N is given per pixel, averaged in the 5,000-5,500Å spectral window. The  $\sigma_1 \dots \sigma_5$  cases represent the bins regarding the velocity dispersion of the satellite galaxy (with the interval quoted underneath in km/s).

ID	$\log \mu \equiv \log M_{\text{SAT}}/M_{\text{PRI}}$	N	$z_M$	Number of spectra (S/N)				
				$\sigma_1$ 100-130	$\sigma_2$ 130-160	$\sigma_3$ 160-190	$\sigma_4$ 190-220	$\sigma_5$ 220-250
$\mu_1$	(-0.278, 0.000]	663	$0.11799 \pm 0.01918$	39 ( 73)	145 (154)	215 (203)	176 (205)	88 (157)
$\mu_2$	(-0.490, -0.278]	669	$0.11143 \pm 0.01846$	110 (114)	231 (195)	190 (192)	82 (135)	56 (114)
$\mu_3$	[-0.800, -0.490]	672	$0.10038 \pm 0.01801$	189 (155)	258 (199)	130 (156)	71 (123)	24 ( 75)
$\mu_0$	[-0.800, 0.000]	2004	$0.10934 \pm 0.01933$	338 (201)	634 (316)	535 (313)	329 (269)	168 (207)

determined from the dust maps of Schlafly & Finkbeiner (2011) – and brought into the rest frame. The spectra are normalized in flux in the wavelength interval 5,000-5,500Å and the resulting flux is drizzled to a reference grid, performing linear interpolation to split the flux between adjacent bins. Two sources of uncertainty must be taken into account: on the one hand, we propagate the statistical uncertainties of individual flux measurements – given by the inverse variance in each entry of the SDSS spectra. Moreover, additional scatter will be expected from the stacking procedure, due to intrinsic variations in the properties of the galaxies whose spectra are stacked. To quantify the latter source of uncertainty, we perform a bootstrap method whereby 100 realizations of each stack are created by selecting each time a random set comprising 75% of the original galaxies within a given subsample (i.e. for a choice of velocity dispersion and stellar mass ratio bin). The resulting standard deviation is added in quadrature to the statistical scatter from individual measurements. We note that the drop in S/N caused by adding this second source of noise (from variance in the galaxy sample within a bin) stays within 10-20% of the ‘intrinsic’ noise obtained from the spectra. This is an important issue, confirming that the galaxy-to-galaxy variance within a velocity dispersion bin does not dominate the error budget. The total S/N for each stack is quoted in Table 1, and given as an average in the rest-frame 5,000-5,500Å spectral window. Moreover, the difference between the final flux values and those that correspond to the median of the distribution of 100 realizations stays below 20% of the final error. Our errors are thus conservative.

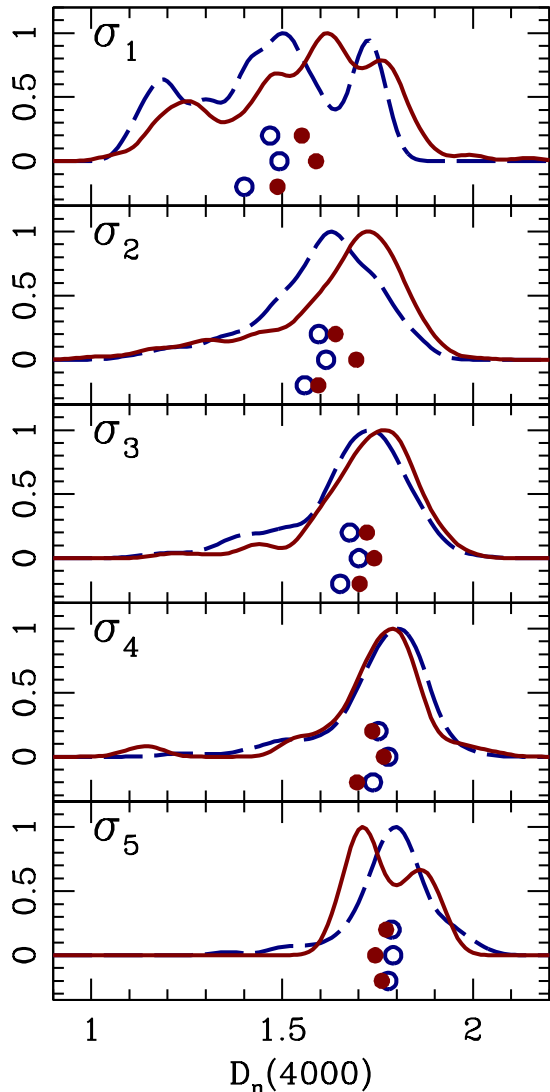
For the comparison among all bins, we decided to bring all the stacked spectra to a common velocity dispersion. Although this technique doubtlessly washes out information from the spectra, our aim is to robustly constrain differences in the populations of satellite galaxies, at fixed stellar mass, with respect to the mass ratio of the pair. Given the range of velocity dispersion of the sample, we chose  $\sigma_0 = 250 \text{ km s}^{-1}$ , as the common value. To do that, we convolve the stacks with a Gaussian kernel, inspecting the result with pPXF (Cappellari & Emsellem 2004) until the output velocity dispersion matches the targeted  $\sigma_0$ . We note the process produces the same, fiducial, velocity dispersion with an uncertainty less than  $\sim 2 \text{ km s}^{-1}$ .

To illustrate the validity of the stacked spectra as a true representative of a subsample, we show in Fig. 3 the distribution of the  $D_n(4000)$  index (as defined in Balogh et al. 1999) measured in *individual* spectra, compared with

the equivalent index measured in the stacked spectra (dots) corresponding to each subsample, shown with respect to velocity dispersion, in increasing order from the top down. The histograms are smoothed following a standard Gaussian Kernel Density Estimator (see, e.g., Chen 2017). In each panel, the symbols show, from top to bottom, the measurement of  $D_n(4000)$  on the stacks, the median, and the mean of the individual measurements, respectively. The blue open and red solid dots represent the  $\mu_1$  and  $\mu_3$  sets, respectively. Despite the substantial scatter in the individual measurements, the trends follow that of the stacked results, thus justifying the use of stacked spectra to compare the subsamples. Note that noisy data will tend to reduce the break strength.

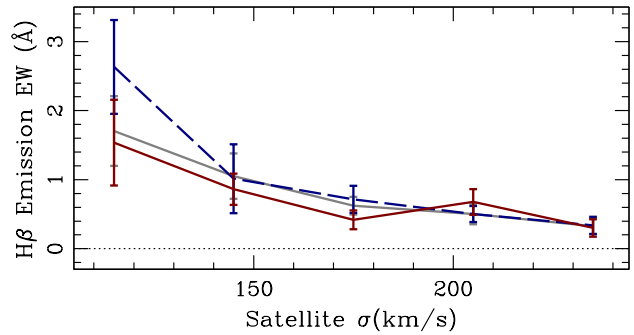
The next step involves removing the contribution from nebular emission. This is especially important in the Balmer lines, because we will be targeting  $H\beta$ ,  $H\gamma$  and  $H\delta$  as key line strength indicators regarding stellar ages. We ran the spectral fitting code STARLIGHT (Cid Fernandes et al. 2005), which performs an MCMC search for a best fit, using mixtures of simple stellar populations. Our base grid comprises a set of 176 SSP spectra from the MILES population synthesis models (Vazdekis et al. 2012), with 44 age steps between 0.1 and 14.1 Gyr and four metallicity bins, namely  $[Z/H]=\{-0.71,-0.40,0.00,+0.22\}$ . The spectra are fit in the region 3,750-7,000 Å. The code includes dust attenuation as an additional parameter, and we made sure the emission line regions were masked out during the fits. The output best-fit spectra are compared with the original one, and a Gaussian fit is performed in eleven spectral regions corresponding to Balmer  $H\alpha$  to  $H\delta$ , [OIII] at 4959 and 5007Å, [NII] at 6548 and 6583Å, and [SII] at 6716 and 6731Å. We use these best-fit Gaussians to remove the flux from the original spectra, and the line strengths are measured on the cleaned spectra. Fig. 4 plots the equivalent width of the emission line correction in the  $H\beta$  line as a function of velocity dispersion, with the dashed blue line (solid red line) representing the  $\mu_1$  ( $\mu_3$ ) stacks. The grey line shows the result for the  $\mu_0$  sample (i.e. no segregation with respect to the mass ratio). Note the monotonically decreasing trend of the emission component with velocity dispersion, and the significantly higher level of emission in the  $\mu_1$  stacks, corresponding to satellites around less massive primaries.

Fig. 5 shows the line strengths of the cleaned spectra at the fiducial  $250 \text{ km s}^{-1}$  velocity dispersion, in the  $\mu_1$  (dashed blue lines) and  $\mu_3$  (solid red lines) subsamples, with respect to the velocity dispersion of each bin. The indices



**Figure 3.** Histograms with the 4000Å break strength measured in *individual* spectra. The histograms are renormalized within each bin ( $\sigma_1 \cdots \sigma_5$ ). The solid red lines correspond to satellites around the most massive primaries (i.e. subset  $\mu_3$ ), and the dashed blue lines represent satellites around lower mass primaries (i.e. subset  $\mu_1$ ). The dots, from bottom to top are the  $D_n(4000)$  measurements of the stacked spectra; the median, and the mean of the individual estimates, respectively. In each case, the blue open dots (red solid dots) represent the  $\mu_1$  ( $\mu_3$ ) subsample.

used in the analysis consist of the standard age-sensitive indicators:  $H\beta_o$  (Cervantes & Vazdekis 2009),  $H\gamma_A$  and  $H\delta_A$  (Worthey & Ottaviani 1997),  $D_n(4000)$  (Balogh et al. 1999), CN2 and G4300 (Trager et al. 1998). We complement the analysis with a set of metallicity-sensitive indicators:  $Mgb$ ,  $\langle Fe \rangle \equiv Fe5270 + Fe5335$ , NaD,  $C_{24668}$ , and  $Ca4227$  (Trager et al. 1998) and  $[MgFe]'$  (Thomas et al. 2003). The data show a consistent local trend from young, possibly metal-poor populations at low velocity dispersion, towards an older, metal-rich composition in the more massive stacks. In addition to this locally-driven trend, we find a consistent environment-related trend, such that *at fixed satellite velocity dispersion*, the  $\mu_1$  sample – involving satellites where the mass



**Figure 4.** Correction for emission in the  $H\beta$  line, measured as an equivalent width. The error bars have been blown up by a factor of 3. The solid red (dashed blue) lines correspond to satellites around the most (least) massive primaries. The grey line is the trend for the stacks comprising all satellites, i.e. not segregated with respect to the mass of the primary galaxy.

ratio  $\mu$  is closer to 1:1, therefore associated to the lowest mass primaries – feature younger populations. This trend is very similar to the one found in Ferreras et al. (2017), who used a different set of spectra assembled from GAMA/AAT data. Moreover, note this behaviour mirrors that of the emission lines in Fig. 4, as the stacks with younger populations also produce higher emission line corrections. This result appears to be quite robust, especially considering that the age-sensitive indices  $D_n(4000)$ , CN2 and G4300 are independent of any nebular emission line correction. Such a trend is quite remarkable, because it shows that the stellar population ages of satellite and primary galaxies in pairs are linked. The cause of such a link is discussed in Section 5. In the next section, we will translate these line strength differences into stellar age trends.

#### 4 EXTRACTING SSP-EQUIVALENT PARAMETERS

When translating the observed line strength differences into variations of the stellar populations, we decided to keep the potential trends as clear cut as possible in this paper. We opted to work with SSP-equivalent variations, namely the observed line strengths are compared with a large volume of single stellar populations over a wide range of ages and metallicities. A more complex set of models based on extended star formation histories complicates the analysis beyond the scope of this paper. Our fundamental aim is to assess whether – in line with our previous findings based on AAT spectra in the GAMA survey – significant differences are found between satellite galaxies with the same velocity dispersion (i.e. the “local driver”), caused by the presence of a nearby massive primary (i.e. the “environment driver”). An SSP-equivalent derivation is not only satisfactory for our purposes, but the quantification of the sought differences are better defined than with extended formation models. However, in order to ascertain that the derived variations are not produced by a model-related systematic, we will consider two completely independent sets of population synthesis models. Our data will be fitted with the standard BC03 models of Bruzual & Charlot (2003) and the

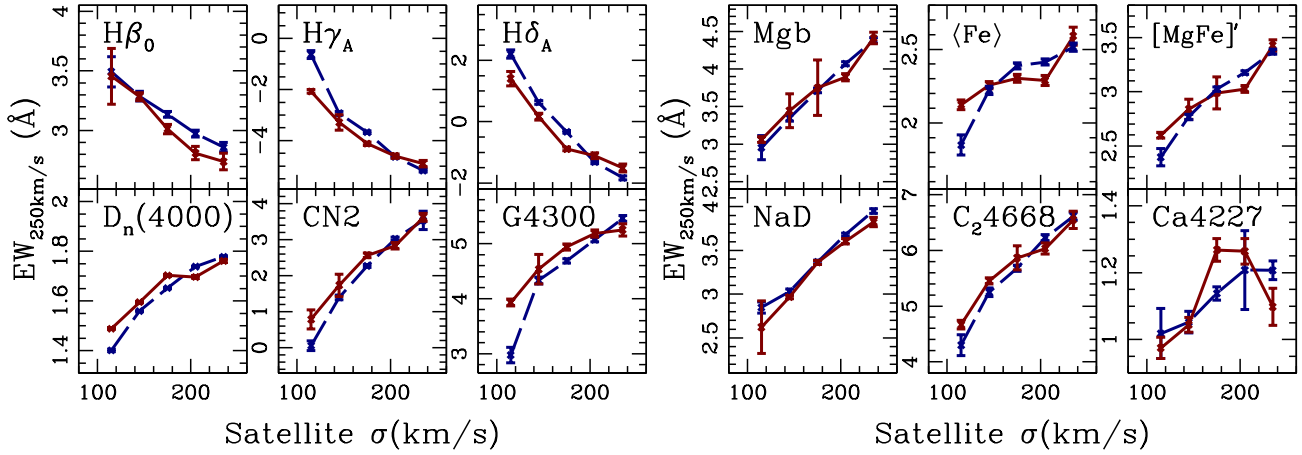


**Figure 5.** Equivalent widths of a number of age- (LHS) and metallicity-sensitive (RHS) spectral features, measured on the stacks. The sample is shown with respect to the measured velocity dispersion of the satellite galaxy (horizontal axis), but the spectra are convolved to a common dispersion of  $250 \text{ km s}^{-1}$ , to assess potential differences. The solid red (dashed blue) lines correspond to satellites around the most (least) massive primaries.

**Table 2.** SSP-equivalent ages of satellite galaxies (in Gyr), including the 68% confidence level. The meaning of the  $\mu$  and  $\sigma$  subsets is shown in Table 1

ID	$\sigma_1$	$\sigma_2$	$\sigma_3$	$\sigma_4$	$\sigma_5$
BC03 models					
$\mu_1$	$1.71^{+0.23}_{-0.48}$	$2.25^{+0.52}_{-0.32}$	$2.70^{+0.39}_{-0.43}$	$3.37^{+0.80}_{-0.44}$	$4.42^{+1.44}_{-0.97}$
$\mu_2$	$1.94^{+0.44}_{-0.53}$	$2.27^{+0.32}_{-0.40}$	$3.19^{+0.84}_{-0.59}$	$4.80^{+1.44}_{-1.06}$	$3.46^{+0.77}_{-0.46}$
$\mu_3$	$1.93^{+0.45}_{-0.48}$	$2.56^{+0.50}_{-0.49}$	$2.99^{+0.61}_{-0.47}$	$3.50^{+0.83}_{-0.59}$	$3.84^{+1.13}_{-0.68}$
$\mu_0$	$1.82^{+0.45}_{-0.48}$	$2.31^{+0.55}_{-0.41}$	$3.01^{+0.69}_{-0.53}$	$3.54^{+0.86}_{-0.58}$	$3.70^{+0.89}_{-0.57}$
MIUSCAT models					
$\mu_1$	$1.67^{+0.19}_{-0.18}$	$2.35^{+0.32}_{-0.32}$	$2.81^{+0.35}_{-0.31}$	$3.60^{+0.91}_{-0.41}$	$4.68^{+0.97}_{-0.83}$
$\mu_2$	$2.22^{+0.29}_{-0.42}$	$2.49^{+0.45}_{-0.39}$	$3.24^{+0.68}_{-0.41}$	$4.82^{+1.14}_{-1.09}$	$3.97^{+1.13}_{-0.52}$
$\mu_3$	$2.19^{+0.20}_{-0.33}$	$2.52^{+0.53}_{-0.52}$	$3.41^{+0.78}_{-0.40}$	$4.02^{+1.27}_{-0.71}$	$3.89^{+1.14}_{-0.44}$
$\mu_0$	$2.05^{+0.25}_{-0.35}$	$2.41^{+0.52}_{-0.40}$	$3.22^{+0.72}_{-0.40}$	$4.13^{+1.17}_{-0.71}$	$4.19^{+1.09}_{-0.57}$

more recent MIUSCAT models of Vazdekis et al. (2012). Not only do these models have different implementations of the isochrones, but they are also based on different stellar libraries.

The ages are derived by comparing the observed line strengths with a grid of SSP models with ages ranging from 0.5 to 14 Gyr in 256 (logarithmic) steps, and from  $[Z/H] = -0.5$  to  $+0.3$  in 64 steps (the MIUSCAT grid only extends out to  $+0.22$  in  $[Z/H]$  as this is the highest available value of metallicity). Both sets adopt a fiducial, Milky Way-like initial mass function (Chabrier 2003 for the BC03 models, and Kroupa 2001 for MIUSCAT). The line strengths of the model grid are compared with the observations with a standard  $\chi^2$  statistic. However, at the high S/N of the stacks (see Table 1), a naive comparison of the line strengths will not be capable of fitting all features consistently. However, we aim at looking for *relative* differences between the stacked spectra. To achieve this goal, we define a fiducial stack – corresponding to  $(\sigma_1, \mu_0)$  – introducing offsets to the

line strengths, so that the fitting procedure gives an acceptable reduced  $\chi^2$  to the fiducial stack. The offsets thus produced, are applied to the rest of the stacks for the analysis. Moreover, these offsets are also added in quadrature to the individual line strengths, so that less weight is given to those indices that require larger modifications. Even though the absolute values of age and metallicity are not to be trusted with this methodology, the relative variations should be robust (when interpreted as SSP-equivalent differences).

Table 2 shows the SSP-equivalent ages for each of the stacks, with the confidence levels quoted at  $1\sigma$ . These results are marginalized with respect to metallicity (using a flat prior over the range of metallicity considered). A clearer assessment of differences with respect to the stellar mass ratio can be seen in Fig. 6, where we show the full 2D probability distribution corresponding to the analysis (from the inside out, the contour plots represent the 1, 2 and  $3\sigma$  confidence levels). While the ages quoted in Table 2 do not show so clearly the difference between stacks  $\mu_1$  and  $\mu_3$  at fixed velocity dispersion, the figure strongly suggests that  $\mu_3$  stacks (i.e. satellites around the most massive hosts) are subtly, but consistently older than their counterparts, *at fixed velocity dispersion*, around lower mass primaries. This effect is most noticeable at low velocity dispersion, with differences in stellar age around  $\sim 0.5$  Gyr, a result consistent with the study based on the GAMA/AAT sample of Ferreras et al. (2017). However, we need to describe in some detail the differences between the sample selection performed here – where velocity dispersion is the main stacking parameter – and the selection adopted in that paper – where stellar mass is the main stacking parameter. Fig. 7 shows the distribution of galaxies in the  $\mu_1$  (dashed blue) and  $\mu_3$  (solid red) subsamples used in this paper, with respect to several observables, as labelled. The mean and standard deviation of the distributions are quantified in Table 3. Note the expected trivial behaviour of the data with respect to velocity dispersion (rightmost panels). The panels concerning the distribution in the mass ratio ( $\log \mu$ ) also show a clear separation between the  $\mu_1$  and  $\mu_3$  subsets. Note that the histograms with respect to either satellite or primary stellar mass reveal that the dif-

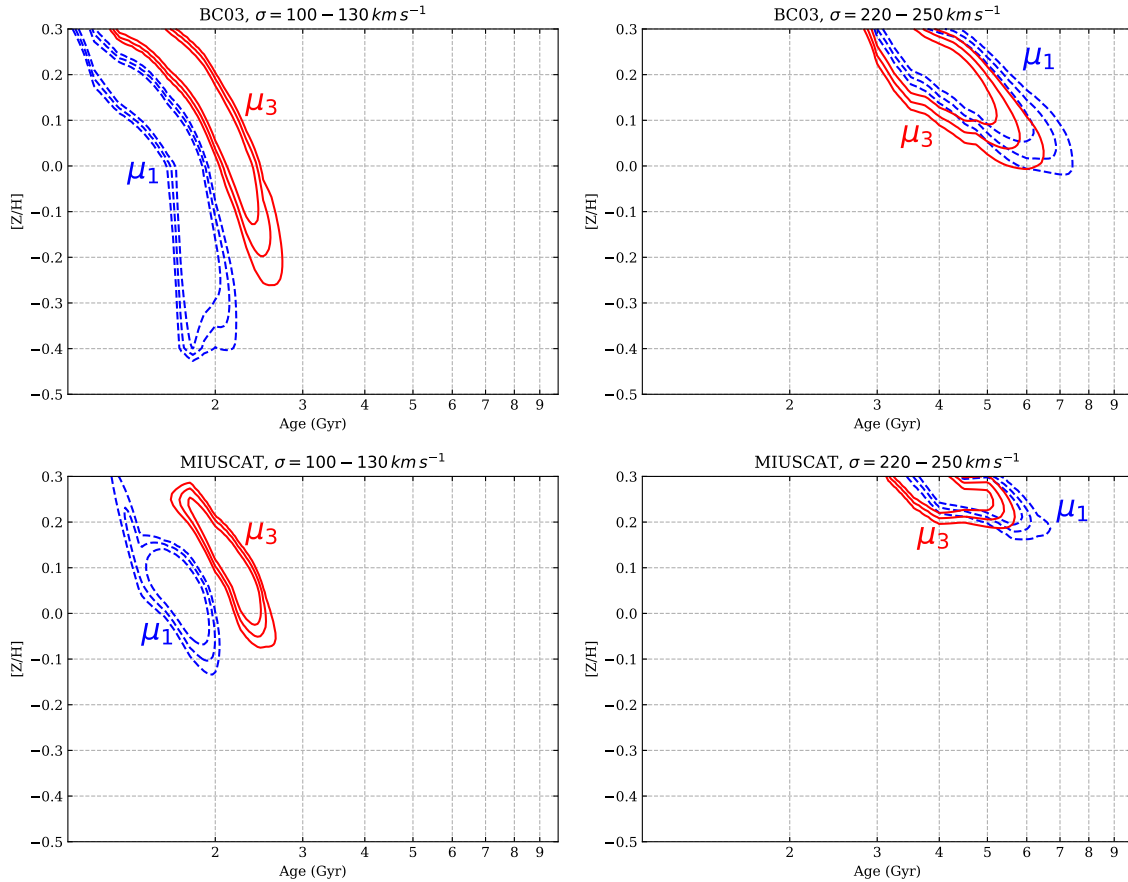


**Figure 6.** Probability maps of the SSP-equivalent age and metallicity. The contour levels are shown at the 1, 2, and 3  $\sigma$  confidence levels (from the inside out) in the  $\mu_1$  (blue dashed lines) and the  $\mu_3$  (solid red lines) subsamples. Two different sets of population synthesis models are used: Bruzual & Charlot (2003, top panels) and MIUSCAT (Vazdekis et al. 2012) models (bottom panels). The two extreme choices of velocity dispersion are shown, as labelled.

ference between these two subsets lies in a complex mixture of satellite and primary masses, such that the  $\mu_3$  (older) subsample consistently represents a distribution where the primary mass is higher than in  $\mu_1$ , but also the satellite mass is *lower* than that of the  $\mu_1$  (i.e. younger) subsample (all at fixed velocity dispersion). We emphasize that velocity dispersion correlates more strongly with the population parameters than stellar mass, and is less prone to systematic uncertainties. Therefore, the results in this paper are more robust than those based on stellar mass, presented in Ferreras et al. (2017). The fact that satellites with lower mass are *older* than the more massive counterparts, when orbiting more massive primaries illustrates the significance of this environment-related trend. Also note that the trend cannot be ascribed to a bias caused by the flux limit imposed on the parent SDSS spectroscopic sample. Such a bias would mainly affect the  $\mu_3$  subset (i.e. lower mass satellites), so that fainter galaxies with the same velocity dispersion – therefore older – would be missed from the stacks. In this case, the analysis would result in even older stellar ages of satellites in the  $\mu_3$  stack, implying that the age difference found here is resilient against incompleteness from the flux-limited sample selection.

Further support for this trend can be found in Fig. 8,

where we show the difference between the  $\mu_3$  and  $\mu_1$  stacks at three choices of velocity dispersion, spanning the full range explored. The difference is quoted as a fraction of the flux in the full sample at a given velocity dispersion, denoted  $\mu_0$  (see Table 1). Note the significant excess of red light in the spectra of the low-mass satellites ( $\sigma_1$ ) associated to the most massive primaries ( $\mu_3$ ). This result is fully consistent with the previous analysis of the line strengths, and confirms the environment-driven stellar age difference. In more detail, note the slight bumps in the  $\sigma_1$  set (bottom panel) at the position of the Balmer lines H $\delta$  (4,100Å) and H $\gamma$  (4,340Å), as expected if  $\mu_3$  satellites were older than those in the  $\mu_1$  subset. Moreover, the dips at the position of the Ca II H and K lines ( $\sim 3,950$ Å), G-band (4,300Å) and Mg complex at 5,200Å are suggestive of a slightly lower metallicity in  $\mu_3$ , but the population analysis presented above (see Fig. 6) confirms that the inherent age-metallicity degeneracy weakens all possible constraints on metallicity. Although much less significant, it did not escape our attention the inversion of the age trend at the highest values of velocity dispersion (rightmost panels of Fig. 6 and  $\sigma_5$  values in Table 2). The age difference is compatible, within error bars, with no variation, but it is worth noting that the  $\mu_3$  satellites become *younger* than the  $\mu_1$  set at the highest velocity dispersion.

**Table 3.** Mean and standard deviation of the distribution of a few properties of the individual galaxies in each stack (see Table 1 for the meaning of the  $\mu$  and  $\sigma$  subindices). The full distributions are presented in Fig. 7.

	$\mu_1$	$\mu_2$	$\mu_3$
$\log(M_{\text{SAT}}/M_{\odot})$			
$\sigma_1$	$10.87 \pm 0.10$	$10.73 \pm 0.12$	$10.53 \pm 0.14$
$\sigma_2$	$10.94 \pm 0.12$	$10.77 \pm 0.14$	$10.61 \pm 0.16$
$\sigma_3$	$10.96 \pm 0.13$	$10.81 \pm 0.12$	$10.69 \pm 0.17$
$\sigma_4$	$11.03 \pm 0.14$	$10.87 \pm 0.14$	$10.73 \pm 0.21$
$\sigma_5$	$11.08 \pm 0.15$	$10.91 \pm 0.16$	$10.84 \pm 0.19$
$\log(M_{\text{PRI}}/M_{\odot})$			
$\sigma_1$	$11.05 \pm 0.07$	$11.12 \pm 0.11$	$11.17 \pm 0.12$
$\sigma_2$	$11.10 \pm 0.10$	$11.15 \pm 0.13$	$11.24 \pm 0.15$
$\sigma_3$	$11.12 \pm 0.11$	$11.19 \pm 0.13$	$11.31 \pm 0.17$
$\sigma_4$	$11.15 \pm 0.12$	$11.25 \pm 0.14$	$11.38 \pm 0.18$
$\sigma_5$	$11.21 \pm 0.14$	$11.30 \pm 0.15$	$11.43 \pm 0.20$
$\log(M_{\text{SAT}}/M_{\text{PRI}})$			
$\sigma_1$	$-0.17 \pm 0.07$	$-0.41 \pm 0.06$	$-0.64 \pm 0.09$
$\sigma_2$	$-0.18 \pm 0.07$	$-0.39 \pm 0.06$	$-0.63 \pm 0.09$
$\sigma_3$	$-0.18 \pm 0.08$	$-0.38 \pm 0.06$	$-0.62 \pm 0.09$
$\sigma_4$	$-0.13 \pm 0.08$	$-0.40 \pm 0.06$	$-0.60 \pm 0.09$
$\sigma_5$	$-0.10 \pm 0.08$	$-0.36 \pm 0.06$	$-0.60 \pm 0.10$
$\sigma/100 \text{ km s}^{-1}$			
$\sigma_1$	$1.19 \pm 0.08$	$1.17 \pm 0.08$	$1.16 \pm 0.09$
$\sigma_2$	$1.50 \pm 0.09$	$1.46 \pm 0.08$	$1.44 \pm 0.09$
$\sigma_3$	$1.74 \pm 0.09$	$1.74 \pm 0.08$	$1.72 \pm 0.09$
$\sigma_4$	$2.04 \pm 0.09$	$2.04 \pm 0.08$	$2.03 \pm 0.08$
$\sigma_5$	$2.31 \pm 0.08$	$2.29 \pm 0.08$	$2.31 \pm 0.07$

## 5 DISCUSSION

The main trend of satellite galaxies being older at fixed velocity dispersion if the mass ratio  $\mu$  is smaller, may be, in principle surprising and counterintuitive, as one generally expects the stellar ages of galaxies to decrease with decreasing mass (e.g. Gallazzi et al. 2005; van de Sande et al. 2018). However, our result can be understood in the context of assembly bias in hierarchical cosmologies (e.g. Sheth & Tormen 2004; Avila-Reese et al. 2005; Gao & White 2007), as lower  $\mu = M_{\text{SAT}}/M_{\text{PRI}}$  ratios are typically associated to older groups, in which all the mergers with the massive primary galaxy have already taken place. This naturally means that groups with low  $\mu$  collapsed earlier than those groups of the same mass with higher  $\mu$  ratios. If that is the case, then it follows that galaxies in groups that collapsed earlier are older than those in dynamically younger groups of the same mass. Extreme examples of the correlation between group age and the central-to-satellite mass ratio are fossil groups and clusters (e.g. Jones et al. 2003; Zarattini et al. 2016), in which the most massive satellite of the system is at least two magnitudes fainter than the central, brightest galaxy. D’Onghia et al. (2005) and Dariush et al. (2010), among others, showed that in a hierarchical universe, these fossil groups are expected to have been formed at much higher redshift than other groups of the same mass.

Recently, Zehavi et al. (2018) used several cosmological semi-analytic models of galaxy formation to study the ef-

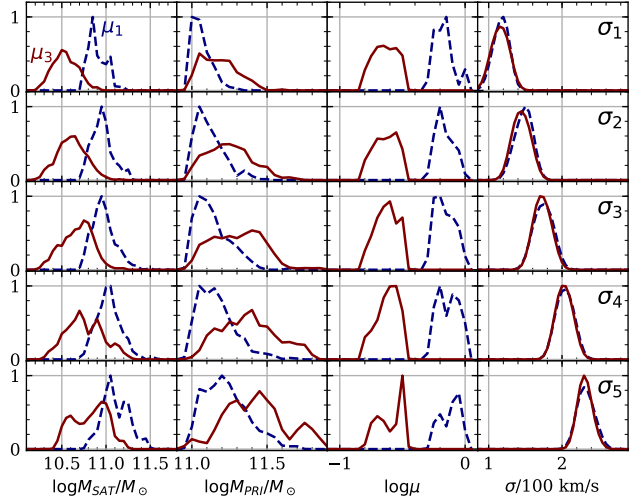


**Figure 7.** Distribution of subsample properties in the  $\mu_1$  (blue dashed histograms) and  $\mu_3$  subsets (solid red histograms). The sample is binned with respect to velocity dispersion, as labelled, in increasing order of  $\sigma$  from the top down. See Tables 1 and 3 for more details.

fect of halo assembly bias on the formation of galaxies and found that at fixed halo mass, older halos (which collapsed earlier) tend to have a smaller number of satellites and with satellite-to-central galaxy mass ratios that are much smaller than younger halos, in line with our findings. Artale et al. (2018), using the cosmological hydrodynamical EAGLE and Illustris simulations (Schaye et al. 2015 and Vogelsberger et al. 2014, respectively) showed that the central galaxies of older halos are more massive than those in younger halos at fixed halo mass by 0.1–0.3 dex. Similar differences in stellar mass were reported by Zehavi et al. (2018). This agrees with what we find in our sample, as the central galaxies of the  $\mu_3$  selection are more massive than those in the  $\mu_1$  set by  $\sim 0.2$  dex. We should also note that the recent analysis of Davies et al. (2019) showed that the passive fraction of satellites increases steeply with decreasing  $M_{\text{SAT}}/M_{\text{PRI}}$  in GAMA, supporting the idea that group age affects the ages and passive fractions of satellite galaxies. All this evidence points towards assembly bias being the plausible origin for the trends we observe. However, to confirm this, simulations would need to mimic our selection, which is based on velocity dispersion of the satellite galaxies. We should emphasize that we refer here to one-halo assembly bias, i.e. concerning galaxies within the same dark matter halo. Alternatively, two-halo assembly bias (see, e.g., Kauffmann et al. 2013; Sin, Lilly, & Henriques 2017; Tinker et al. 2018) affects the properties over larger scales (beyond 1 Mpc), and is not related to the claimed effect (see the review of Wechsler & Tinker 2018, especially their section 6.2, for more details on this distinction).

## 6 SUMMARY

The properties of close pairs involving a massive galaxy can be used to understand the growth mechanisms via mergers, as well as the role of environment in galaxy formation.



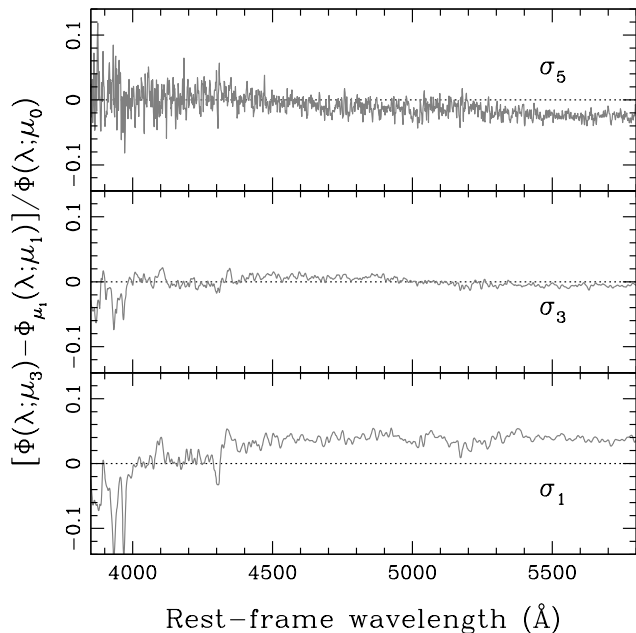


**Figure 8.** Spectral difference between the stacks for  $\mu_3$  and  $\mu_1$  at three values of the velocity dispersion, as labelled (see Table 1 for the interpretation of the  $\mu$  and  $\sigma$  subsamples). The difference is quoted as a fraction of the flux in the general  $\mu_0$  set. Note the significant excess of red light in the  $\mu_3$  stack at low velocity dispersion (bottom panel), a result that is consistent with the older ages obtained in the targeted line strength analysis, with respect to the  $\mu_1$  subsample.

This paper extends the work of Ferreras et al. (2017), based on GAMA/AAT spectra, to a different sample of high S/N spectra from the Sloan Digital Sky Survey. The methodology is very similar to that paper, selecting nearby companions of massive galaxies, in dynamical interaction leading to a potential merger. Here we use the stellar velocity dispersion of the satellite as a “local” proxy, and the satellite-to-primary mass ratio,  $\mu$ , to characterize the close pair. Very high S/N spectra are created by stacking the data in a set of five bins in velocity dispersion and three bins in mass ratio, with a careful selection of redshift, to avoid systematic trends (Fig. 2). The working sample comprises about two thousand high quality SDSS spectra – in the redshift window  $0.07 < z < 0.14$  – covering a velocity dispersion between 100 and  $250 \text{ km s}^{-1}$  and a satellite-to-primary stellar mass ratio between 1:6 and 1:1 (Table 1).

A battery of spectral line strengths is studied to assess the difference in stellar age between satellites involving different values of the mass ratio, at fixed velocity dispersion (Fig. 5). Were environment-related processes irrelevant, we would have found no difference in the underlying populations of the stacks with respect to the mass ratio,  $\mu$ . In agreement with our GAMA-based analysis, we find a consistent trend, such that satellites around the most massive galaxies are systematically older (based on SSP-equivalent ages, see Fig. 6 and Table 2), with the age difference increasing towards decreasing velocity dispersion, up to 0.5 Gyr at the lowest velocity dispersions probed ( $\sigma \sim 100 \text{ km s}^{-1}$ ). This result provides yet another supporting argument of galactic conformity (Weinmann et al. 2006) and the idea of a galaxy

assembly bias (Hearin et al. 2015), such that satellites with low values of the mass ratio  $\mu$ , are expected to lie in halos that form earlier, akin to a fossil group.

## ACKNOWLEDGEMENTS

IF acknowledges support from the AAO through their distinguished visitor programme, as well as funding from the Royal Society. Funding for SDSS-III has been provided by the Alfred P. Sloan Foundation, the Participating Institutions, the National Science Foundation, and the U.S. Department of Energy Office of Science. The SDSS-III web site is <http://www.sdss3.org/>.

## REFERENCES

- Abolfathi B., et al., 2018, *ApJS*, 235, 42  
 Artale M. C., Zehavi I., Contreras S., Norberg P., 2018, *MNRAS*, 480, 3978  
 Avila-Reese V., Colín P., Gottlöber S., Firmani C., Mautbertsch C., 2005, *ApJ*, 634, 51  
 Balogh M. L., Morris S. L., Yee H. K. C., Carlberg R. G., Ellingson E., 1999, *ApJ*, 527, 54  
 Barone T. M., et al., 2018, *ApJ*, 856, 64  
 Bernardi M., et al., 2003, *AJ*, 125, 1882  
 Bray A. D., et al., 2016, *MNRAS*, 455, 185  
 Bruzual G., Charlot S., 2003, *MNRAS*, 344, 1000  
 Cappellari, M., Emsellem, E., 2004, *PASP*, 116, 138  
 Cardelli J. A., Clayton G. C., Mathis J. S., 1989, *ApJ*, 345, 245  
 Cervantes J. L., Vazdekis A., 2009, *MNRAS*, 392, 691  
 Chabrier G., 2003, *PASP*, 115, 763  
 Chen, Y.-C., 2017, *Biostatistics & Epidemiology*, 1, 161  
 Cid Fernandes R., Mateus A., Sodré L., Stasińska G., Gomes J. M., 2005, *MNRAS*, 358, 363  
 Conselice C. J., 2014, *ARA&A*, 52, 291  
 Dariush A. A., Raychaudhury S., Ponman T. J., Khoshroshahi H. G., Benson A. J., Bower R. G., Pearce F., 2010, *MNRAS*, 405, 1873  
 Davies L. J. M., et al., 2019, *MNRAS*, in press  
 de La Rosa I. G., La Barbera F., Ferreras I., de Carvalho R. R., 2011, *MNRAS*, 418, L74  
 D’Onghia E., Sommer-Larsen J., Romeo A. D., Burkert A., Pedersen K., Portinari L., Rasmussen J., 2005, *ApJ*, 630, L109  
 Driver S. P., et al., 2011, *MNRAS*, 413, 971  
 Ellison S. L., Patton D. R., Simard L., McConnachie A. W., 2008, *AJ*, 135, 1877  
 Ferreras I., et al., 2014, *MNRAS*, 444, 906  
 Ferreras I., et al., 2017, *MNRAS*, 468, 607  
 Gallazzi A., Charlot S., Brinchmann J., White S. D. M., Tremonti C. A., 2005, *MNRAS*, 362, 41  
 Gao L., Springel V., White S. D. M., 2005, *MNRAS*, 363, L66  
 Gao L., White S. D. M., 2007, *MNRAS*, 377, L5  
 Goddard, D., et al., 2016, *MNRAS*, 465, 688  
 Graves G. J., Faber S. M., Schiavon R. P., 2009, *ApJ*, 693, 486  
 Greene, J. E., et al., 2015, *ApJ*, 807, 11  
 Greene, J. E., et al., 2013, *ApJ*, 776, 64

- Hartley, W., Conselice, C. J., Mortlock, A., Foucaud, S., Simpson, C., 2015, *MNRAS*, 451, 1613
- Hearin, A. P., Watson, D. F., van den Bosch, F. C., 2015, *MNRAS*, 452, 1958
- Jones, L. R.; Ponman, T. J.; Horton, A.; Babul, A.; Ebeling, H.; Burke, D. J., 2003, *MNRAS*, 343, 627
- Kauffmann, G., et al., 2003, *MNRAS*, 341, 33
- Kauffmann G., Li C., Zhang W., Weinmann S., 2013, *MNRAS*, 430, 1447
- Kaviraj S., 2014, *MNRAS*, 437, L41
- Kawinwanichakij L., et al., 2016, *ApJ*, 817, 9
- Kroupa P., 2001, *MNRAS*, 322, 231
- La Barbera F., Ferreras I., de Carvalho R. R., Bruzual G., Charlot S., Pasquali A., Merlin E., 2012, *MNRAS*, 426, 2300
- Lin, L., et al., 2004, *ApJ*, 617, L9
- López-Sanjuan C., et al., 2012, *A&A*, 548, A7
- Mármol-Queraltó E., Trujillo I., Pérez-González P. G., Varela J., Barro G., 2012, *MNRAS*, 422, 2187
- Naab T., Johansson P. H., Ostriker J. P., 2009, *ApJ*, 699, L178
- Oser L., Naab T., Ostriker J. P., Johansson P. H., 2012, *ApJ*, 744, 63
- Pahwa I., Paranjape A., 2017, *MNRAS*, 470, 1298
- Paranjape A., Kovač K., Hartley W. G., Pahwa I., 2015, *MNRAS*, 454, 3030
- Patton D. R., Carlberg R. G., Marzke R. O., Pritchett C. J., da Costa L. N., Pellegrini P. S., 2000, *ApJ*, 536, 153
- Pérez-González P. G., et al., 2013, *ApJ*, 762, 46
- Rogers, B., Ferreras, I., Kaviraj, S., Pasquali, A., Sarzi, M., 2009, *MNRAS*, 399, 2172
- Ruiz P., Trujillo I., Mármol-Queraltó E., 2014, *MNRAS*, 442, 347
- Schaye J., et al., 2015, *MNRAS*, 446, 521
- Schlafly E. F., Finkbeiner D. P., 2011, *ApJ*, 737, 103
- Scott N., et al., 2017, *MNRAS*, 472, 2833
- Sheth R. K., Tormen G., 2004, *MNRAS*, 350, 1385
- Sin L. P. T., Lilly S. J., Henriques B. M. B., 2017, *MNRAS*, 471, 1192
- Sol Alonso, M., Tissera, P. B., Coldwell, G., Lambas, D. G., 2004, *MNRAS*, 352, 1081
- Thomas D., Maraston C., Bender R., 2003, *MNRAS*, 339, 897
- Thomas D., Maraston C., Bender R., Mendes de Oliveira C., 2005, *ApJ*, 621, 673
- Tinker J. L., Hahn C., Mao Y.-Y., Wetzel A. R., Conroy C., 2018, *MNRAS*, 477, 935
- Trager S. C., Worthey G., Faber S. M., Burstein D., González J. J., 1998, *ApJS*, 116, 1
- Treyer M., et al., 2018, *MNRAS*, 477, 2684
- van de Sande J., et al., 2018, *NatAs*, 2, 483
- Vazdekis A., Ricciardelli E., Cenarro A. J., Rivero-González J. G., Díaz-García L. A., Falcón-Barroso J., 2012, *MNRAS*, 424, 157
- Vogelsberger M., et al., 2014, *MNRAS*, 444, 1518
- Wechsler R. H., Tinker J. L., 2018, *ARA&A*, 56, 435
- Weinmann S. M., van den Bosch F. C., Yang X., Mo H. J., 2006, *MNRAS*, 366, 2
- Worthey G., Ottaviani D. L., 1997, *ApJS*, 111, 377
- Zarattini S., et al., 2016, *A&A*, 586, A63
- York D. G., et al., 2000, *AJ*, 120, 1579
- Zehavi I., Contreras S., Padilla N., Smith N. J., Baugh C. M., Norberg P., 2018, *ApJ*, 853, 84
- Zu Y., Mandelbaum R., 2018, *MNRAS*, 476, 1637